



HAL
open science

Optimal bispectrum estimator and simulations of the CMB lensing-integrated Sachs Wolfe non-Gaussian signal

A. Mangilli, B. Wandelt, F. Elsner, M. Liguori

► **To cite this version:**

A. Mangilli, B. Wandelt, F. Elsner, M. Liguori. Optimal bispectrum estimator and simulations of the CMB lensing-integrated Sachs Wolfe non-Gaussian signal. *Astronomy and Astrophysics - A&A*, 2013, 555, 10.1051/0004-6361/201321433 . hal-03645534

HAL Id: hal-03645534

<https://hal.science/hal-03645534>

Submitted on 11 Aug 2022

HAL is a multi-disciplinary open access archive for the deposit and dissemination of scientific research documents, whether they are published or not. The documents may come from teaching and research institutions in France or abroad, or from public or private research centers.

L'archive ouverte pluridisciplinaire **HAL**, est destinée au dépôt et à la diffusion de documents scientifiques de niveau recherche, publiés ou non, émanant des établissements d'enseignement et de recherche français ou étrangers, des laboratoires publics ou privés.

Optimal bispectrum estimator and simulations of the CMB lensing-integrated Sachs Wolfe non-Gaussian signal

A. Mangilli¹, B. Wandelt^{1,2}, F. Elsner¹, and M. Liguori³

¹ Institut d'Astrophysique de Paris et Université Pierre et Marie Curie Paris 6, 98bis Bd. Arago, 75014 Paris, France
e-mail: mangilli@iap.fr

² International Chair of Theoretical Cosmology, Lagrange Institute (ILP), 98bis boulevard Arago, 75014 Paris, France

³ INFN, Sezione di Padova and Dipartimento di Fisica e Astronomia G. Galilei, Università degli Studi di Padova, via Marzolo 8, 35131 Padova, Italy

Received 7 March 2013 / Accepted 16 May 2013

ABSTRACT

We present the tools to optimally extract the lensing-integrated Sachs Wolfe (L-ISW) bispectrum signal from future cosmic microwave background (CMB) data. We implemented two different methods to simulate the non-Gaussian CMB maps with the L-ISW signal: a non-perturbative method based on the FLINTS lensing code and the separable mode-expansion method. We implemented the Komatsu, Spergel, and Wandelt (KSW) optimal estimator analysis for the L-ISW bispectrum and tested it on the non-Gaussian simulations for realistic CMB experimental settings with an inhomogeneous sky coverage. We show that the estimator approaches the Cramer-Rao bound and that Wiener filtering the L-ISW simulations slightly improves the estimate of $f_{\text{NL}}^{\text{L-ISW}}$ by $\leq 10\%$. For a realistic CMB experimental setting that accounts for anisotropic noise and masked sky, we show that the linear term of the estimator is highly correlated to the cubic term and it is necessary to recover the signal and the optimal error bars. We also show that the L-ISW bispectrum, if not correctly accounted for, yields an underestimation of the $f_{\text{NL}}^{\text{local}}$ error bars of $\simeq 4\%$. A joint analysis of the non-Gaussian shapes and/or L-ISW template subtraction is needed to recover unbiased results of the primordial non-Gaussian signal from ongoing and future CMB experiments.

Key words. cosmic background radiation

1. Introduction

One of the most relevant mechanisms that can generate non-Gaussianity from secondary cosmic microwave background (CMB) anisotropies is the coupling between weak lensing and the integrated Sachs Wolfe (ISW, [Sachs & Wolfe 1967](#)) and the Rees Sciama (RS) effects ([Rees & Sciama 1968](#)). This correlation gives in fact the leading contribution to the CMB secondary bispectrum with a blackbody frequency dependence ([Goldberg & Spergel 1999](#); [Verde & Spergel 2002](#); [Giovi et al. 2005](#)). Weak lensing of the CMB is caused by gradients in the matter gravitational potential that distorts the CMB photon geodesics. The ISW and the RS effects, on the other hand, are related to the time variation of the gravitational potential wells. The relevant mechanism is given by the late ISW, owing to the action of dark energy, which causes the decay of the gravitational potential wells as the Universe expands. Both the lensing and the ISW effect are therefore related to the matter gravitational potential and thus are correlated phenomena. This gives rise to a non-vanishing three-point correlation function or, analogously, a non-vanishing bispectrum, its Fourier counterpart. The RS (also referred to as the non-linear ISW) arises when the growth of structure in the evolving universe becomes non-linear. Because it is a second-order effect, the RS gives a smaller contribution to the signal than the ISW. The CMB bispectrum arising from the cross-correlation between lensing and ISW/RS (from now on referred to as L-ISW) is expected to have a high signal-to-noise ratio from ongoing and future CMB experiments so that it will be detectable in the near future with a high statistical

significance ([Verde & Spergel 2002](#); [Giovi et al. 2005](#); [Mangilli & Verde 2009](#); [Lewis et al. 2011](#)). A detection would open the possibility to exploit the cosmological information related to the late-time evolution encoded in the L-ISW signal. It is useful to stress that a significant detection of the L-ISW signal from ongoing CMB experiments such as *Planck* would be a powerful probe of dark energy from the CMB alone and would be a complementary probe of the late-time Universe with respect to the large scale structure and the CMB power spectrum analysis. Moreover, [Mangilli & Verde \(2009\)](#) and [Hanson et al. \(2009\)](#) showed that the L-ISW bispectrum can be a serious contaminant for estimating the primary local non-Gaussianity from future data. Ongoing CMB experiment such as *Planck* ([Planck Collaboration 2011](#)) and future experiments such as CORe ([The CORe Collaboration et al. 2011](#)) will therefore require a detailed reconstruction of the L-ISW bispectrum either to be able to correctly remove the L-ISW contribution when estimating the local primary non-Gaussian parameter f_{NL} , or to exploit the cosmological information encoded in the signal; therefore it becomes extremely important to know how to model and simulate it.

We present the formalism and numerical implementation i) to generate simulated CMB maps containing the L-ISW signal and ii) to build and test the optimal estimator for the L-ISW bispectrum, accounting for both the cubic and the linear parts. The linear part for this specific kind of signal has been calculated and tested here for the first time. We implemented and tested the L-ISW signal with two methods for the CMB non-Gaussian simulations: the separable mode-expansion method

(Fergusson et al. 2010; Smith & Zaldarriaga 2011) and the non-perturbative approach described in Sect. 2.1.

It is important to have an optimal estimator for the L-ISW bispectrum to extract the signal optimally from future data and to separate it from other types of non-Gaussianities, i.e. the local primary bispectrum, with which it is degenerated. Here, following Komatsu (2010) and Munshi et al. (2011), we implemented the KSW bispectrum estimator (Komatsu et al. 2005) for the L-ISW signal of a full sky, cosmic-variance-limited CMB experiment and a more realistic instrumental setting, similar to that of a space-based experiment. Furthermore, for this realistic case, we investigated the statistical detection significance and the impact that the L-ISW bispectrum has on the estimation and on the variance of the primary local non-Gaussian parameter f_{NL} .

The outline of this paper is as follows. In Sect. 2 we present the methods for simulating the non-Gaussian CMB maps that contain the L-ISW bispectrum signal by using both the separable mode-expansion method and the non-perturbative covariance method. Section 3 provides the basics for building and implementing the optimal estimator for the L-ISW signal, including its linear part. It also includes a discussion of the implementation of the Wiener-filtered simulation algorithm. In Sect. 4 we present the relevant tests and results. In Sect. 5 we quantify the statistical detection significance of the L-ISW bispectrum and the impact on the error of primary non-Gaussianity f_{NL} due to the presence of the ISW signal. Finally, in Sect. 6, we discuss the results and summarize the conclusions. Details on the simulations built with the covariance method and on the L-ISW cross-correlation coefficients are given in the appendix.

2. Simulated non-Gaussian CMB maps

In this section, we present the formalism for creating simulated CMB maps for the L-ISW bispectrum. We used two different methods: a non-perturbative approach, here named the ‘‘covariance method’’, and the separable mode-expansion method (Fergusson et al. 2010 and Smith & Zaldarriaga 2011). The latter provides an efficient and easy to handle way of generating L-ISW maps, while the former method provides better insights into the physics related to the L-ISW bispectrum. In this case, in fact, the L-ISW signal is generated starting from the covariance matrix that represents the expected correlation between the lensing and the ISW/RS effects.

2.1. Covariance method

The L-ISW correlation is defined by the covariance matrix,

$$\mathbf{C}_{\text{L-ISW}} = \begin{pmatrix} C_{\ell}^{\phi\phi} & C_{\ell}^{T\phi} \\ C_{\ell}^{T\phi} & C_{\ell}^{TT} \end{pmatrix} \quad (1)$$

and the cross-correlation coefficient,

$$r^{T\phi} = \frac{C_{\ell}^{T\phi}}{\sqrt{C_{\ell}^{TT}} \sqrt{C_{\ell}^{\phi\phi}}}. \quad (2)$$

Here, $C_{\ell}^{TT} \delta_{\ell\ell'} \delta_{mm'} = \langle a_{\ell m}^{\text{P}} a_{\ell' m'}^{\text{P}*} \rangle$ and $C_{\ell}^{\phi\phi} \delta_{\ell\ell'} \delta_{mm'} = \langle \phi_{\ell m}^{\text{L}} \phi_{\ell' m'}^{\text{L}*} \rangle$ are the CMB primary temperature power spectrum and the lensing power spectrum, where the lensing potential ϕ (the gravitational potential projection along the line of sight) is defined by

$$\phi(\hat{\mathbf{n}}) = -2 \int_0^{r_{\text{ls}}} dr \frac{r(z_{\text{ls}}) - r(z)}{r(z) r(z_{\text{ls}})} \Phi(r, \hat{\mathbf{n}}r). \quad (3)$$

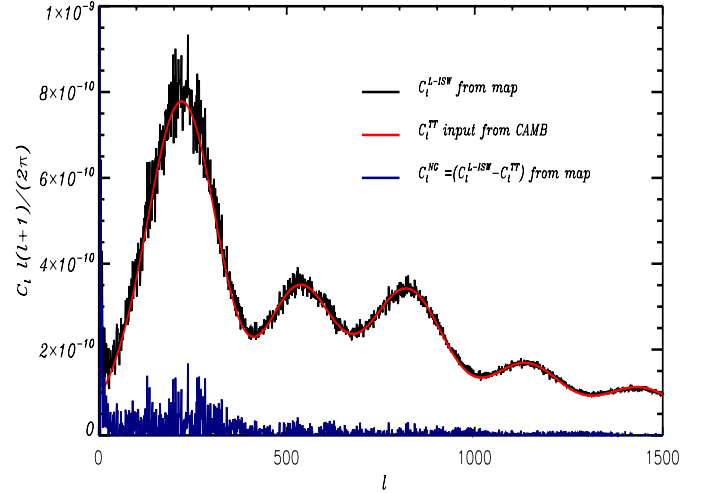


Fig. 1. L-ISW power spectrum from the covariance method simulation. The plot shows that the temperature power spectrum of the L-ISW simulations generated with the method described in Sect. 2.1 is compatible with the input theoretical power spectrum from CAMB and that the non-Gaussian contribution is always subdominant. The temperature power spectrum from one simulated L-ISW realization is shown in black, the red line refers to the theoretical input from CAMB while the blue refers to the non-Gaussian L-ISW contribution from the same realization.

The term in the numerator, $C_{\ell}^{T\phi}$, is the power spectrum of the cross-correlation between the lensing and the ISW/RS effect, see Appendix B for details.

After a Cholesky decomposition of the L-ISW correlation matrix $\mathbf{C}_{\text{L-ISW}}$, the two new variables $t_{\ell m}$ and $z_{\ell m}$ are defined by

$$t_{\ell m} = \sqrt{C_{\ell}^{\phi\phi}} x_{\ell m} \equiv \phi_{\ell m}^{\text{L}} \quad (4)$$

$$z_{\ell m} = \sqrt{C_{\ell}^{TT}} [x_{\ell m} r^{T\phi} + y_{\ell m} \sqrt{1 - (r^{T\phi})^2}], \quad (5)$$

where $x_{\ell m}$ and $y_{\ell m}$ are two independent random Gaussian fields. By definition, the new fields are such that: $\langle t^2 \rangle = C_{\ell}^{\phi\phi}$, $\langle z^2 \rangle = C_{\ell}^{TT}$ and they have the non-zero cross-correlation $\langle zt \rangle = C_{\ell}^{T\phi}$.

As described in Appendix A, the map that contains the desired L-ISW bispectrum is given by the coefficients

$$a_{\ell m}^{\text{L-ISW}} = z_{\ell m} + a_{\ell m}^{\text{L}} - a_{\ell m}^{\text{P}} \equiv z_{\ell m} + \Delta a_{\ell m}^{\text{L}}, \quad (6)$$

where $a_{\ell m}^{\text{P}}$ and $a_{\ell m}^{\text{L}}$ are the unlensed primary and the lensing angular coefficients, and $\Delta a_{\ell m}^{\text{L}} = a_{\ell m}^{\text{L}} - a_{\ell m}^{\text{P}}$ corresponds to the lensing expansion terms only. Note that by construction $y_{\ell m}$ has the same phases as $a_{\ell m}^{\text{P}} \equiv y_{\ell m} \sqrt{C_{\ell}^{TT}}$ and $\phi_{\ell m}^{\text{L}} \equiv x_{\ell m} \sqrt{C_{\ell}^{\phi\phi}}$ the same as $x_{\ell m}$, which is necessary for building a map with the desired bispectrum signal.

Figure 1 shows in black the temperature CMB power spectrum of one simulated L-ISW map, $C_{\ell}^{\text{L-ISW}}$, built from Eq. (6). The non-Gaussian contribution, in blue in the figure, is always subdominant and the $C_{\ell}^{\text{L-ISW}}$ are consistent with the theoretical input $(C_{\ell}^{TT})_{\text{th}}$ (red line) obtained with CAMB (Lewis et al. 2000)¹. As throughout the paper, the reference cosmological model used is the Λ CDM model with parameter values defined in Komatsu et al. (2011).

¹ <http://camb.info>

2.2. Separable mode-expansion method

Following Fergusson et al. (2010) and Smith & Zaldarriaga (2011), the non-Gaussian part of the CMB angular coefficients can be defined starting from a given reduced bispectrum. For the L-ISW signal, the method can be used because this kind of signal is separable, so that

$$[a_{\ell m}^{\text{NG}}]_{\text{L-ISW}} = \int d^2\hat{n} \sum_{\ell_2 m_2 \ell_3 m_3} b_{\ell_1 \ell_2 \ell_3}^{\text{L-ISW}} Y_{\ell}^m(\hat{n}) \times \frac{a_{\ell_2 m_2}^G Y_{\ell_2}^{m_2}(\hat{n}) a_{\ell_3 m_3}^G Y_{\ell_3}^{m_3}(\hat{n})}{C_{\ell_2} C_{\ell_3}}. \quad (7)$$

From the expression of the L-ISW reduced bispectrum in Eq. (13) and by factorizing the ℓ dependence, the explicit form of the non-Gaussian contribution to the $a_{\ell m}$ from the L-ISW cross correlation is given by

$$[a_{\ell m}^{\text{NG}}]_{\text{L-ISW}} = \frac{1}{6} \int d^2\hat{n} Y_{\ell}^m(\hat{n}) [\ell(\ell+1)Q(\hat{n})E(\hat{n}) + C_{\ell}([\delta^2 E](\hat{n})Q(\hat{n}) - [\delta^2 Q](\hat{n})E(\hat{n})) - ([\delta^2 P](\hat{n})Q(\hat{n}) + [\delta^2 Q](\hat{n})P(\hat{n})) - \ell(\ell+1)Q(\hat{n})P(\hat{n}) + q_{\ell}([\delta^2 E](\hat{n})P(\hat{n}) - [\delta^2 P](\hat{n})E(\hat{n})) + \ell(\ell+1)q_{\ell}P(\hat{n})E(\hat{n})]. \quad (8)$$

Here,

$$\begin{aligned} P(\hat{n}) &\equiv \sum_{\ell m} a_{\ell m} Y_{\ell m}(\hat{n}), \\ Q(\hat{n}) &\equiv \sum_{\ell m} C_{\ell}^{T\phi} (C^{-1}a)_{\ell m} Y_{\ell m}(\hat{n}), \\ E(\hat{n}) &\equiv \sum_{\ell m} (C^{-1}a)_{\ell m} Y_{\ell m}(\hat{n}). \end{aligned} \quad (9)$$

The maps with a δ^2 prefix are given by, e.g., $\delta^2 P = -\sum_{\ell} \ell(\ell+1) a_{\ell m} Y_{\ell m}(\hat{n})$; they correspond to the maps of Eq. (10) multiplied by the $-\ell(\ell+1)$ factor. The final solution containing the L-ISW signal is

$$a_{\ell m} = a_{\ell m}^G + [a_{\ell m}^{\text{NG}}]_{\text{L-ISW}}, \quad (10)$$

where $a_{\ell m}^G$ is the Gaussian part.

In Fig. 2, we show the CMB temperature power spectra from the Gaussian and the non-Gaussian map, as defined in Eq. (8). The non-Gaussian contribution is always subdominant, as expected.

3. The optimal KSW estimator for the lensing-ISW/RS bispectrum

In this section we present the formalism for the KSW estimator (Komatsu et al. 2005) for the L-ISW bispectrum signal.

3.1. Definition

The $a_{\ell m}$ probability distribution function (PDF) in the limit of weak non-Gaussianity (i.e., truncated at the bispectrum level) is

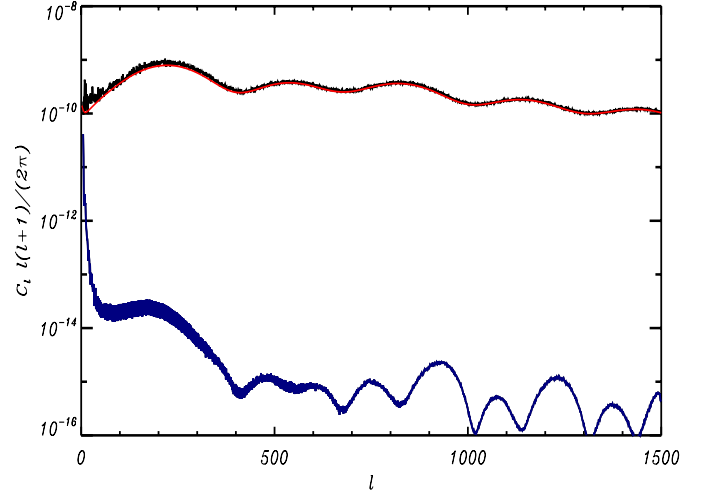


Fig. 2. L-ISW power spectrum from the separable mode-expansion method simulation. The temperature power spectrum of the L-ISW simulation generated with the method described in Sect. 2.2 is compatible with the input theoretical power spectrum from CAMB and the non-Gaussian contribution is always subdominant. The temperature power spectrum from one simulated L-ISW realization is shown in black, the red line refers to the theoretical input from CAMB while the blue refers to the non-Gaussian L-ISW contribution from the same realization.

given by (Babich 2005; Taylor & Watts 2001; Komatsu 2010)

$$\begin{aligned} P(a) &= \frac{1}{(2\pi)^{N_{\text{harm}}/2} |C|^{1/2}} \exp \left[-\frac{1}{2} \sum_{\ell m} \sum_{\ell' m'} a_{\ell m}^* (C^{-1})_{\ell m, \ell' m'} a_{\ell' m'} \right] \\ &\times \left\{ 1 + \frac{1}{6} \sum_{\text{all } \ell_1 m_1 \ell_2 m_2 \ell_3 m_3} \langle a_{\ell_1 m_1} a_{\ell_2 m_2} a_{\ell_3 m_3} \rangle \left[(C^{-1}a)_{\ell_1 m_1} (C^{-1}a)_{\ell_2 m_2} (C^{-1}a)_{\ell_3 m_3} \right. \right. \\ &\left. \left. - 3 (C^{-1})_{\ell_1 m_1, \ell_2 m_2} (C^{-1}a)_{\ell_3 m_3} \right] \right\}. \end{aligned} \quad (11)$$

where $\langle a_{\ell_1 m_1} a_{\ell_2 m_2} a_{\ell_3 m_3} \rangle$ is the *angular bispectrum*. Here, we are interested in the L-ISW case, for which the angular bispectrum, parametrized by the amplitude parameter $f_{\text{NL}}^{\text{L-ISW}}$, is

$$\langle a_{\ell_1 m_1} a_{\ell_2 m_2} a_{\ell_3 m_3} \rangle = \mathcal{G}_{\ell_1 \ell_2 \ell_3}^{m_1 m_2 m_3} f_{\text{NL}}^{\text{L-ISW}} b_{\ell_1 \ell_2 \ell_3}^{\text{L-ISW}}, \quad (12)$$

where

$$b_{\ell_1 \ell_2 \ell_3}^{\text{L-ISW}} = \left[\frac{\ell_1(\ell_1+1) - \ell_2(\ell_2+1) + \ell_3(\ell_3+1)}{2} C_{\ell_1}^P C_{\ell_3}^{T\phi} + (5p) \right], \quad (13)$$

is the reduced bispectrum and $C_{\ell}^{T\phi} \equiv \langle \phi_{\ell m}^* a_{\ell m}^{\text{L-ISW}} \rangle$ are the L-ISW cross-correlation coefficients. According to Komatsu et al. (2005), for a small departure from Gaussianity, the optimal estimator for the L-ISW amplitude parameter is given by

$$f_{\text{NL}}^{\text{L-ISW}} = (F^{-1}) S_{\text{L-ISW}}, \quad (14)$$

where (F^{-1}) is the inverse of the L-ISW Fisher matrix

$$F \equiv F^{\text{L-ISW}} = f_{\text{sky}} \sum_{2 \leq \ell_1 \leq \ell_2 \leq \ell_3} \frac{B_{\ell_1 \ell_2 \ell_3}^{\text{L-ISW}} B_{\ell_1 \ell_2 \ell_3}^{\text{L-ISW}}}{\Delta_{\ell_1 \ell_2 \ell_3} C_{\ell_1} C_{\ell_2} C_{\ell_3}}. \quad (15)$$

For a realistic CMB experimental setting, the noise, N_{ℓ} , and the beam window function, w_{ℓ} , are accounted for so that $C_{\ell} = N_{\ell} + C_{\ell}^{\text{th}} w_{\ell}^2$. In this case, the bispectrum is also convolved with

the beam transfer function w_ℓ , $B_{\ell_1\ell_2\ell_3}^{\text{L-ISW}} \propto b_{\ell_1\ell_2\ell_3}^{\text{L-ISW}} w_{\ell_1} w_{\ell_2} w_{\ell_3}$. For a mask $M(p)$, the observed sky fraction f_{sky} is defined as

$$f_{\text{sky}} = \frac{\sum_p M(p)}{N_{\text{pix}}}, \quad (16)$$

where $N_{\text{pix}} = 12N_s^2$ is the number of pixels in the map, N_s is the map resolution, and the sum \sum_p is done over the pixels.

Assuming that the only relevant non-Gaussian contribution is coming from the L-ISW term, which is the case if the local primordial non-Gaussianity is small and foregrounds and point sources have been correctly removed and masked, $S_{\text{L-ISW}}$ is given by the data as

$$S_{\text{L-ISW}} \equiv \frac{1}{6} \sum_{\text{all } lm} \mathcal{G}_{\ell_1\ell_2\ell_3}^{m_1m_2m_3} b_{\ell_1\ell_2\ell_3}^{\text{L-ISW}} \left[(C^{-1}a)_{\ell_1m_1} (C^{-1}a)_{\ell_2m_2} (C^{-1}a)_{\ell_3m_3} - 3(C^{-1})_{\ell_1m_1, \ell_2m_2} (C^{-1}a)_{\ell_3m_3} \right]. \quad (17)$$

By factorizing the ℓ_i dependence, this becomes (Komatsu 2010)

$$S_{\text{L-ISW}} = \frac{1}{2} \int d^2\hat{n} \left\{ P(\hat{n}) [\delta^2 E](\hat{n}) Q(\hat{n}) - [\delta^2 P](\hat{n}) E(\hat{n}) Q(\hat{n}) - P(\hat{n}) E(\hat{n}) [\delta^2 Q](\hat{n}) \right\} + S_{\text{lin}}^{\text{ISW}}, \quad (18)$$

where the maps $P(\hat{n})$, $E(\hat{n})$, $Q(\hat{n})$ etc. are the same as defined in Eqs. (10) and, in the case of a realistic experiment, they are convolved with the experimental window function w_ℓ so that, for example, $P(\hat{n}) \equiv \sum_{\ell m} w_\ell a_{\ell m} Y_{\ell m}(\hat{n})$.

In Eq. (18), the first two lines refer to the cubic part of the estimator, while $S_{\text{lin}}^{\text{L-ISW}}$ is the linear part, which corrects for anisotropies and must be included if rotational invariance is not preserved. Details on the analytic expression of the L-ISW linear term and on its numerical implementation are given in the next Sect. 3.2 and in Sect. 4.

3.2. Linear term

The linear term of the estimator is given by

$$S_{\text{lin}}^{\text{L-ISW}} = -\frac{1}{2} \int d^2\hat{n} \sum_{\text{all } lm} b_{\ell_1\ell_2\ell_3}^{\text{L-ISW}} \times (C^{-1})_{\ell_1m_1, \ell_2m_2} (C^{-1}a)_{\ell_3m_3} Y_{\ell_1}^{m_1}(\hat{n}) Y_{\ell_2}^{m_2}(\hat{n}) Y_{\ell_3}^{m_3}(\hat{n}). \quad (19)$$

By using the explicit form of $b_{\ell_1\ell_2\ell_3}^{\text{L-ISW}}$ and by factorizing the ℓ -dependence, one obtains

$$S_{\text{lin}}^{\text{L-ISW}} = -\frac{1}{2} \int d^2\hat{n} \left\{ Q(\hat{n}) \left[\langle P(\hat{n}) \delta^2 E(\hat{n}) \rangle_{\text{MC}} - \langle E(\hat{n}) \delta^2 P(\hat{n}) \rangle_{\text{MC}} \right] - \delta^2 Q(\hat{n}) \langle P(\hat{n}) E(\hat{n}) \rangle_{\text{MC}} - E(\hat{n}) \left[\langle Q(\hat{n}) \delta^2 P(\hat{n}) \rangle_{\text{MC}} + \langle P(\hat{n}) \delta^2 Q(\hat{n}) \rangle_{\text{MC}} \right] + \delta^2 E(\hat{n}) \langle P(\hat{n}) Q(\hat{n}) \rangle_{\text{MC}} - \delta^2 P(\hat{n}) \langle E(\hat{n}) Q(\hat{n}) \rangle_{\text{MC}} + P(\hat{n}) \left[\langle Q(\hat{n}) \delta^2 E(\hat{n}) \rangle_{\text{MC}} - \langle E(\hat{n}) \delta^2 Q(\hat{n}) \rangle_{\text{MC}} \right] \right\}, \quad (20)$$

where $\langle \rangle_{\text{MC}}$ indicates the Monte Carlo (MC) averages and the different maps are defined in Eq. 10. They are convolved with the experimental window function w_ℓ , so that $P(\hat{n}) \equiv \sum_{\ell m} w_\ell a_{\ell m} Y_{\ell m}(\hat{n})$, etc.

3.3. Wiener-filtered maps

The optimal bispectrum estimator as described in Eqs. (17) and (18) involves products of inverse-variance-filtered maps, $C^{-1}a = (S + N)^{-1}a$, where S and N are the signal and the noise covariance matrix, respectively. A brute-force calculation of such an expression is impractical for modern high-resolution experiments because it involves the inversion of two matrices that are too large to be stored and processed as dense systems. If the noise covariance can be described in terms of a simple power spectrum in spherical harmonic space, the calculation simplifies significantly. However, this approach is no longer exact for experiments with anisotropic noise distribution or reduced sky coverage, leading to an increase in the error bars of the estimates.

Here, we used Wiener filtering as a basis for the exact evaluation of terms involving $C^{-1}a$. We applied the iterative scheme of Elsner & Wandelt (2013) to calculate the Wiener filter $a^{\text{WF}} \equiv S(S + N)^{-1}a$, the maximum a posteriori solution if signal and noise are Gaussian random fields. After a^{WF} has been successfully computed, we finally obtain the inverse-variance-filtered map by normalizing the spherical harmonic coefficients of the Wiener-filter solution by the CMB power spectrum multiplied with the beam window function, $C^{-1}a_{\ell m} = (C_\ell^{\text{th}} b_\ell^2)^{-1} a_{\ell m}^{\text{WF}}$.

4. Results

In this section we present the results for the numerical implementation of the optimal estimator and the methods presented in Sects. 2.1 and 2.2 to build the CMB maps that contain the L-ISW bispectrum. In particular, we processed the simulated L-ISW maps through the estimator pipeline to obtain the amplitude parameter $f_{\text{NL}}^{\text{L-ISW}}$ of Eq. (14). We considered two main settings:

- a full-sky cosmic-variance-limited CMB experiment up to a maximum multipole $\ell_{\text{max}} \simeq 1000$, and
- a more realistic experimental setting that consisted of a one-channel CMB experiment with a Gaussian beam with a FWHM $\theta_b = 7'$, a galactic mask leaving $\simeq 80\%$ of the sky, and anisotropic uncorrelated noise. These settings are visualized in Figs. C.3, C.2 and details are given in Sect. C.

All runs have been performed at full resolution $N_{\text{side}} = 2048$ (which corresponds to a map pixel number of 5.033×10^7). The maps in Eqs. (10) were calculated with the Healpix package (Gorski et al. 2005). The theoretical power spectrum of the temperature-only primary CMB coefficients C_ℓ was generated with the CAMB code for a fiducial ΛCDM cosmological model with parameters corresponding to WMAP7 cosmological parameters (Komatsu et al. 2011). For illustrative purpose, the plots of the maps and the corresponding ℓ -filters that contain the L-ISW cross-correlation coefficients $C_\ell^{T\phi}$ are shown in Figs. 3 and 4.

We built a set of 100 CMB simulations for each of the two methods described in sections 2.2 and 2.1 for a cosmic-variance-limited CMB experiment with full sky coverage. For the covariance method, we used the FLINTS code (Lavaux & Wandelt 2010) to generate the lensing coefficients $a_{\ell m}^{\text{L}}$ and the lensing potential coefficients $\phi_{\ell m}$ needed to build the non-Gaussian $a_{\ell m}^{\text{L-ISW}}$ as described in Sect. 2.1. In both cases, we analyzed the L-ISW simulated CMB maps with the L-ISW estimator up to $\ell_{\text{max}} = 1000$. According to the definition of $f_{\text{NL}}^{\text{L-ISW}}$, the expected value is 1 with 1σ error predicted from theory for $\ell_{\text{max}} = 1000$ of $\simeq 0.64$. For the separable expansions mode method, the simulations give a mean $f_{\text{NL}}^{\text{L-ISW}} = 1.1$ with averaged 1σ error $\simeq 0.69$.

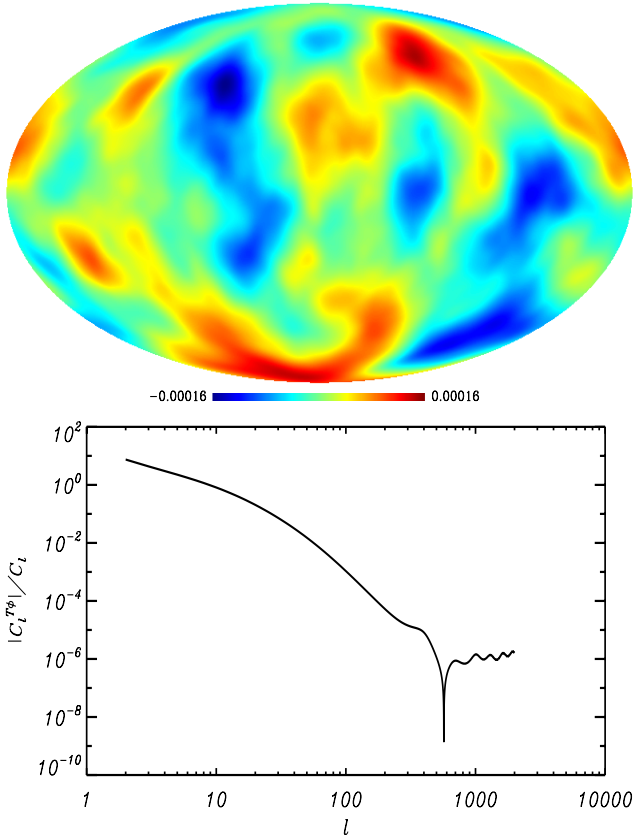


Fig. 3. Large-scale contribution to the non-Gaussian L-ISW signal. *Upper panel:* the map $Q(\hat{n}) \equiv \sum_{\ell m} C_\ell^{T\phi} (C^{-1}a)_{\ell m} Y_{\ell m}(\hat{n})$ contains the L-ISW coefficients $C_\ell^{T\phi}$ and enters the L-ISW estimator Eq. (18). The ℓ -filter $\frac{C_\ell^{T\phi}}{C_\ell}$ acts as a filter that suppresses the small scales (*lower panel*).

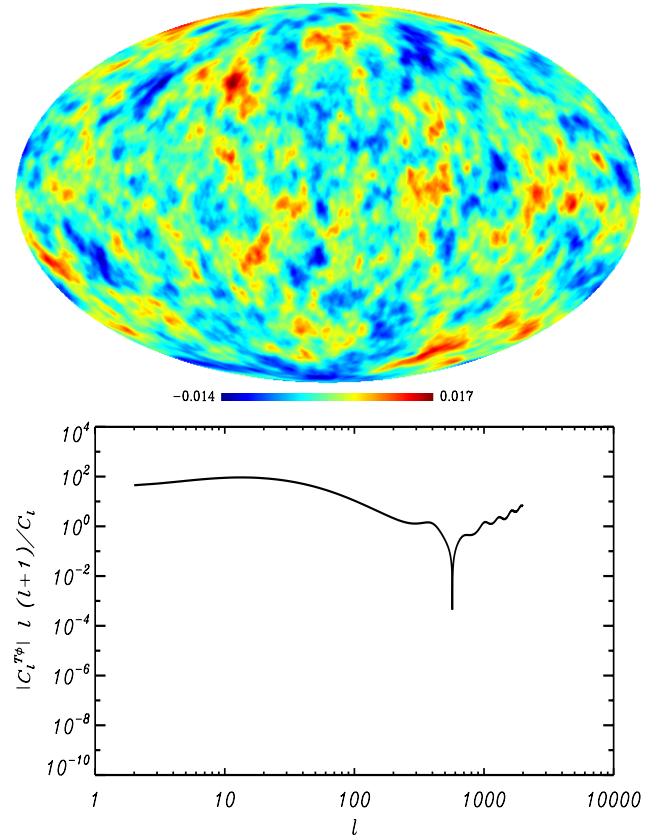


Fig. 4. Intermediate-scale contribution to the non-Gaussian L-ISW signal. Same as Fig. 3 but, for the map $\delta^2 Q = -\sum_{\ell} \ell(\ell+1) C_\ell^{T\phi} (C^{-1}a)_{\ell m} Y_{\ell m}(\hat{n})$ (*upper panel*) and its corresponding filter $-\ell(\ell+1) \frac{C_\ell^{T\phi}}{C_\ell}$. The factor $\ell(\ell+1)$ dominates at high ℓ , defining more small-scale features than the previous Q map.

With the simulations built with the covariance method, we obtain a mean $f_{\text{NL}}^{\text{L-ISW}} = 1.21$ with averaged 1σ error of 0.67. The results are summarized in Figs. 6 and 5. These estimates are compatible with the theoretical predictions. The error bars are slightly sub-optimal because of numerical noise and the fact that we assumed a diagonal covariance matrix so that $(C^{-1}a)_{\ell m} = a_{\ell m}/C_\ell$.

To test the estimator on a more realistic case, we built a set of 100 simulations with the separable mode-expansion method considering a realistic experimental setting. This consists of a CMB one-channel experiment with a Gaussian beam FWHM $\theta_b = 7'$, a galactic mask with $f_{\text{sky}} = 0.78$, and anisotropic noise, as previously described. In this case, we run the estimator up to $\ell_{\text{max}} = 1500$. The expected theoretical 1σ error on $f_{\text{NL}}^{\text{L-ISW}}$ for this experimental setting and up to $\ell_{\text{max}} = 1500$ is ≈ 0.49 . This estimate accounts for a $\approx 10\%$ percent increase in the error bar because the lensing is intrinsically non-Gaussian and gives an extra contribution to the variance, as shown in Lewis et al. (2011). We obtain a mean $f_{\text{NL}}^{\text{L-ISW}} = 1.09$ with averaged 1σ error ≈ 0.55 . In this case we computed both the cubic and linear part of the estimator. In particular, the linear term has been tested with a set of 100 Monte Carlo (MC) averages generated for each map product in equation (Eq. (21)). In the presence of anisotropic noise and a sky cut, the linear part of the estimator is necessary to recover the expected estimation of $f_{\text{NL}}^{\text{L-ISW}}$ and error bars. The linear contribution to $f_{\text{NL}}^{\text{L-ISW}}$ is strongly anti-correlated with the cubic part. This behavior is summarized in Fig. 8. In the plot are shown the linear and the cubic contributions to the total amplitude $f_{\text{NL}}^{\text{L-ISW}} \equiv (f_{\text{NL}}^{\text{L-ISW}})_{\text{cubic}} + (f_{\text{NL}}^{\text{L-ISW}})_{\text{linear}}$. We also checked

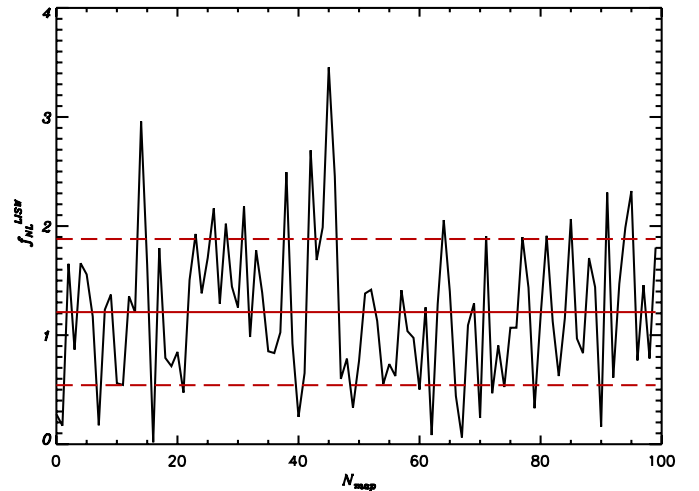


Fig. 5. $f_{\text{NL}}^{\text{L-ISW}}$ values for 100 simulated non-Gaussian maps obtained with the covariance method of Sect. 2.1. The lensing part has been computed with the FLINTS code (Lavaux & Wandelt 2010). The straight line refers to the averaged $f_{\text{NL}}^{\text{L-ISW}}$ from these simulations, the dashed line to the averaged 1σ error. Here $\ell_{\text{max}} = 1000$.

that with 100 MC averages the linear term converges and is stable: for this specific experimental setting we find that the results do not improve when increasing the MC averages to 200.

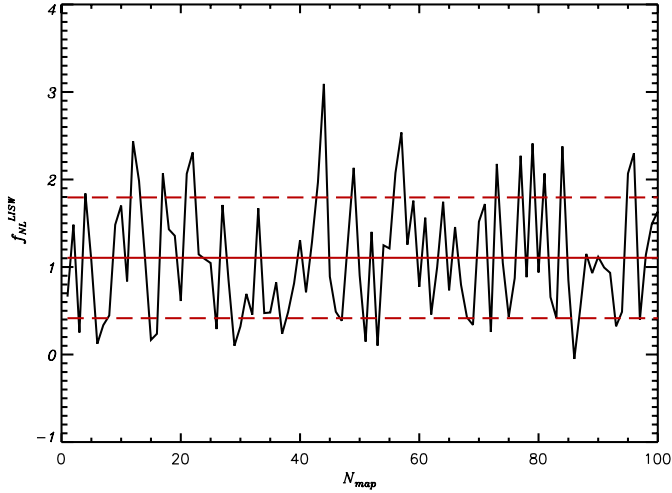


Fig. 6. Same as Fig. 5, but for 100 simulations built with the separable mode-expansion method (Eq. (8)).

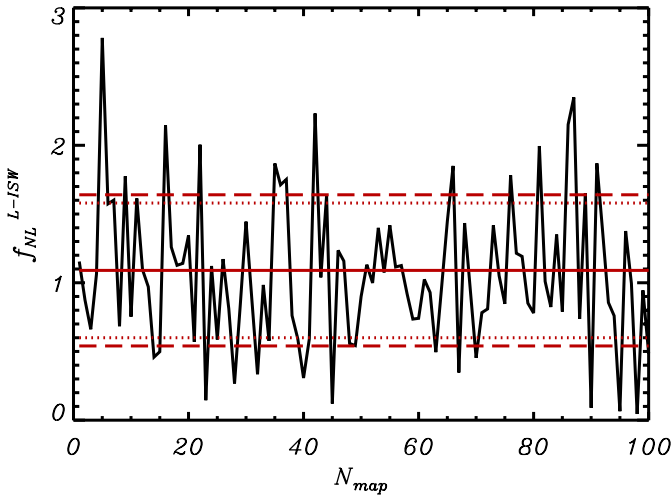


Fig. 7. Same as Fig. 6 but for a more realistic CMB experiment with a 7' FWHM Gaussian beam, anisotropic noise, and a 20% galactic mask. Here $\ell_{\max} = 1500$. The dashed lines are the 1σ averaged error bars from simulations, while the dotted lines are the expected Fisher errors.

Finally, to test optimality, we Wiener-filtered the 100 L-ISW simulations and processed them through the L-ISW estimator pipeline. The maps were produced following [Elsner & Wandelt \(2013\)](#), as described in section Sect. 3.3. We used the same experimental settings as inputs as was described previously. The linear term was computed with 100 Wiener-filtered MC simulations. We found that the improvement over the non Wiener filtered simulations is small ($<10\%$) for our particular settings. However, this does not exclude that the Wiener filtering may have a more noticeable impact for a more realistic experimental setting and noise covariance.

5. f_{NL} error estimation

This section summarizes the results for the impact of the L-ISW signal on the error estimation of f_{NL} from the local-type non-Gaussianity. If the only contribution to f_{NL} were coming from the primary local-type non-Gaussianity, the error on this parameter would be simply given by

$$\sigma^{\text{P}} = \sqrt{\frac{1}{F^{\text{P}}}}, \quad (21)$$

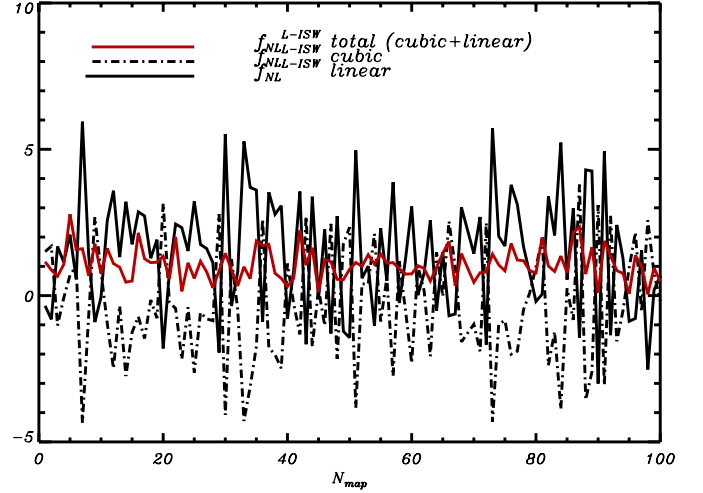


Fig. 8. The linear term of the estimator reduces the error bars for anisotropic data. The plot shows the linear (solid black line) and the cubic (dot-dashed black line) contributions to the total (red line) $f_{\text{NL}}^{\text{L-ISW}} \equiv (f_{\text{NL}}^{\text{L-ISW}})_{\text{cubic}} + (f_{\text{NL}}^{\text{L-ISW}})_{\text{linear}}$ for a CMB experiment with anisotropic noise and a 22% galactic mask.

i.e., the inverse of the Fisher matrix of the local-type non-Gaussian contribution

$$F^{\text{P}} = f_{\text{sky}} \sum_{2 \leq \ell_1 \leq \ell_2 \leq \ell_3} \frac{B_{\ell_1 \ell_2 \ell_3}^{\text{P}} B_{\ell_1 \ell_2 \ell_3}^{\text{P}}}{\Delta_{\ell_1 \ell_2 \ell_3} C_{\ell_1} C_{\ell_2} C_{\ell_3}}, \quad (22)$$

where f_{sky} refers to the observed sky fraction. The noise, N_{ℓ} , and the beam, b_{ℓ} , can be accounted for, so that $C_{\ell} = N_{\ell} + C_{\ell}^{\text{th}} b_{\ell}^2$. In this case the bispectrum is also convolved with the beam transfer function b_{ℓ} : $B_{\ell_1 \ell_2 \ell_3}^{\text{P}} \propto b_{\ell_1 \ell_2 \ell_3}^{\text{P}} b_{\ell_1} b_{\ell_2} b_{\ell_3}$.

However, the L-ISW can be a serious contaminant of the local primary signal ([Mangilli & Verde 2009](#); [Hanson et al. 2009](#)), so that it is important to quantify the effect on the expected f_{NL} error as well. If the L-ISW signal is present, the error matrix will be given by a non-diagonal Fisher matrix of the form

$$F_{ij} = \begin{pmatrix} F^{\text{P}} & F^{\text{cross}} \\ F^{\text{cross}} & F^{\text{L-ISW}} \end{pmatrix}, \quad (23)$$

where

$$F^{\text{cross}} = f_{\text{sky}} \sum_{2 \leq \ell_1 \leq \ell_2 \leq \ell_3} \frac{B_{\ell_1 \ell_2 \ell_3}^{\text{L-ISW}} B_{\ell_1 \ell_2 \ell_3}^{\text{P}}}{\Delta_{\ell_1 \ell_2 \ell_3} C_{\ell_1} C_{\ell_2} C_{\ell_3}} \quad (24)$$

is the cross-correlation term and $F^{\text{L-ISW}}$ is the the Fisher term of the L-ISW signal of Eq. (15). The expected error on the local f_{NL} is

$$\sigma_{\text{cross}}^{\text{P}} = \sqrt{(F^{-1})_{11}}, \quad (25)$$

i.e., the inverse of the full Fisher matrix containing the cross-correlation between the primary local non-Gaussianity and the L-ISW signal. The difference between the error estimation on f_{NL} -primary with and without the L-ISW contribution is

$$\Delta \sigma^{\text{P}} = \sigma_{\text{cross}}^{\text{P}} - \sigma^{\text{P}}. \quad (26)$$

To quantify the level of correlation between the two signals, one can define the correlation coefficient as

$$r = \frac{F^{\text{cross}}}{\sqrt{F^{\text{P}}} \sqrt{F^{\text{L-ISW}}}}. \quad (27)$$

We found that the effect of the local non-Gaussianity on the L-ISW is negligible. Therefore, the $1 - \sigma$ error of the L-ISW amplitude parameter $f_{\text{NL}}^{\text{L-ISW}}$ is given by $\sigma^{\text{L-ISW}} = \sqrt{(F^{\text{L-ISW}})^{-1}}$.

For a realistic CMB experiment as described in Sect. 4 and in Appendix C, we found that the correlation between the two signals is $r = 0.20$ at $\ell_{\text{max}} = 1500$, and $r = 0.27$ at $\ell_{\text{max}} = 2000$, and that the expected detection significance of the L-ISW signal ($1/\sigma^{\text{L-ISW}}$) is at ≈ 2 and $\approx 3\sigma$. The effect on the f_{NL} local error due to the contamination is in the range between $\approx 3\%$ to $\approx 5\%$ for ℓ_{max} from 1000 to 2000, depending on how strongly the two signals are correlated. For $\ell_{\text{max}} = 2000$, if the L-ISW signal is not accounted for correctly, the f_{NL} error bars are overestimated by $\approx 4\%$.

6. Discussion and conclusions

We have presented the formalism and numerical implementation to build the optimal KSW estimator for the lensing-integrated Sachs Wolfe (L-ISW) bispectrum. Moreover, we have tested the estimator on simulated CMB maps containing the L-ISW non-Gaussian signal and on the Wiener-filtered simulations to test optimality. We implemented and tested two methods for the simulations: a non-perturbative approach to simulate CMB sky maps with the L-ISW signal, which is based on the FLINTS lensing code (Lavaux & Wandelt 2010), and the perturbative separable mode-expansion method calculated for this specific signal. We provided the analytical expression and numerical implementation of the linear term of the estimator for this specific type of bispectrum. For a realistic CMB experimental setting that accounts for anisotropic noise and masked sky, the linear term gives a relevant contribution that is highly anti-correlated with the cubic part, and it is necessary to recover the signal and optimal error bars. To achieve optimality, we also tested the estimator on the Wiener-filtered L-ISW-simulated CMB maps. In this case we recovered the signal with error bars that saturate the theoretical Cramer-Rao bound, with a small improvement of $<10\%$ with respect to the non-Wiener-filtered simulations. Finally, we estimated that, if not correctly accounted for, the L-ISW effect also has an impact on $f_{\text{NL}}^{\text{local}}$ error bars, leading to a bias and an overestimation of $\approx 4\%$, in agreement with Lewis et al. (2011). Thus a joint analysis of non-Gaussian shapes and/or L-ISW template subtraction will be needed to recover unbiased minimum variance results of the local-type primordial non-Gaussian signal. The unbiased non-Gaussian results for the local shape from *Planck* data can be found in Planck Collaboration (2013a). A detailed description of different methods for an unbiased analysis of CMB non-Gaussianity can be found in Kim et al. (2013). After subtracting the L-ISW bispectrum signal, there is no evidence of primordial local non-Gaussianity in *Planck* data, since $f_{\text{NL}}^{\text{local}} = 2.7 \pm 5.8$ (Planck Collaboration 2013a). It is important to note that the KSW bispectrum approach to the estimation of the L-ISW is complementary to the lensing reconstruction estimator of Lewis et al. (2011). In principle, the KSW estimator can offer advantages over other methods because the bispectrum has a unique shape and has been shown to be robust to foreground contamination (Yadav & Wandelt 2010), therefore it can be measured by using a larger sky fraction. In addition, including the L-ISW in the framework of bispectrum analysis gives an unified approach to testing for primordial non-Gaussianity. The tools presented here enable the optimal analysis of this important signal from CMB data and can be used for the *Planck* data analysis as described in Planck Collaboration (2013a,b). The L-ISW signal is detected at 2.7σ in the *Planck* temperature data, and we expect that the statistical significance will be increased by $\approx 15\%$

when adding the polarization data. As pointed out in Lewis et al. (2011), the L-ISW bispectrum signal is expected to be detected at $\approx 9\sigma$ by combining the temperature and polarization data from future CMB full-sky and cosmic-variance-limited experiments such as CoRE.

Acknowledgements. This work was supported in part by NSF grants AST 07-08849 and AST 09-08902, and by NASA/JPL subcontract 1413479; and through Ben Wandelt's ANR Chaire d'excellence ANR-10-CEXC-004-01. A.M. acknowledges Guilhem Lavaux for the FLINTS lensing simulations, Licia Verde for useful comments and discussion, and the University of Illinois for the use of the curvaton computers.

Appendix A: simulated L-ISW CMB bispectrum from the covariance method

This appendix describes the covariance method used to build the L-ISW simulated maps and described in Sect. 2.1. It is straightforward to check that the coefficients $a_{\ell m}^{\text{L-ISW}} = z_{\ell m} + \Delta a_{\ell m}^{\text{L}}$ give the desired bispectrum by calculating $\langle (a_{\ell m}^{\text{L-ISW}})^3 \rangle = \langle (z_{\ell m} + \Delta a_{\ell m}^{\text{L}})^3 \rangle$. The lensing coefficients $a_{\ell m}^{\text{L}}$ can be expressed analytically, at first order in the lensing expansion, as

$$a_{\ell m}^{\text{L}} = a_{\ell m}^{\text{P}} + \sum_{\ell' \ell'' m' m''} (-1)^{m+m'+m''} \mathcal{G}_{\ell \ell' \ell''}^{-m m' m''} \times \frac{\ell'(\ell'+1) - \ell(\ell+1) + \ell''(\ell''+1)}{2} a_{m' \ell' m''}^{\text{P}*} \phi_{\ell'' - m''}^{\text{L}}, \quad (\text{A.1})$$

where $a_{\ell m}^{\text{P}}$ the primary and $\phi_{\ell m}^{\text{L}}$ the harmonic coefficients of the lensing potential ϕ^{L} . Since, according to the new variables definition ($z_{\ell m}, t_{\ell m}$) of Eq. (6), $t_{\ell m} = \phi_{\ell m}^{\text{L}}$, the $a_{\ell m}^{\text{L}}$ can be written as

$$a_{\ell m}^{\text{L}} \propto a_{\ell m}^{\text{P}} + f_{\ell} a_{\ell m}^{\text{P}*} t_{\ell m}. \quad (\text{A.2})$$

Here, to simplify the notation, $f_{\ell} = \sum_{\ell' \ell'' m' m''} (-1)^{m+m'+m''} \mathcal{G}_{\ell \ell' \ell''}^{-m m' m''} \frac{\ell'(\ell'+1) - \ell(\ell+1) + \ell''(\ell''+1)}{2}$, so that $\Delta a_{\ell m}^{\text{L}} = f_{\ell} a_{\ell m}^{\text{P}*} t_{\ell m}$ at first order. The explicit expression for $\langle (a_{\ell m}^{\text{L-ISW}})^3 \rangle$ takes the form

$$\langle (a_{\ell m}^{\text{L-ISW}})^3 \rangle = \langle (z_{\ell m} + \Delta a_{\ell m}^{\text{L}})^3 \rangle = \langle z_{\ell m}^3 + z_{\ell m} (\Delta a_{\ell m}^{\text{L}})^2 + 3z_{\ell m}^2 \Delta a_{\ell m}^{\text{L}} + (\Delta a_{\ell m}^{\text{L}})^3 + 2z_{\ell m} (\Delta a_{\ell m}^{\text{L}})^2 \rangle. \quad (\text{A.3})$$

From this the only non-zero term is

$$\langle 3z_{\ell m}^2 \Delta a_{\ell m}^{\text{L}} \rangle = 3 \left\langle f_{\ell} a_{\ell m}^{\text{P}*} t_{\ell m} C_{\ell}^{\text{TT}} \left(x_{\ell m} x_{\ell' m'} (r_{\ell}^{\text{T}\phi})^2 + y_{\ell m} y_{\ell' m'} \times \left(1 - (r_{\ell}^{\text{T}\phi})^2 \right) \right) + 2x_{\ell m} r_{\ell}^{\text{T}\phi} y_{\ell' m'} \sqrt{1 - (r_{\ell}^{\text{T}\phi})^2} \right\rangle. \quad (\text{A.4})$$

From this only survives

$$6 \left\langle f_{\ell} a_{\ell m}^{\text{P}*} t_{\ell m} C_{\ell}^{\text{TT}} x_{\ell m} r_{\ell}^{\text{T}\phi} y_{\ell' m'} \sqrt{1 - (r_{\ell}^{\text{T}\phi})^2} \right\rangle. \quad (\text{A.5})$$

By using the definition of $r_{\ell}^{\text{T}\phi}$ in Eq. (2) and the approximation $r_{\ell}^{\text{T}\phi} \ll 1$ for which $1 - (r_{\ell}^{\text{T}\phi})^2 \approx 1$, since by construction $a_{\ell m}^{\text{P}} = y_{\ell m} \sqrt{C_{\ell}^{\text{TT}}}$, $t_{\ell m} = x_{\ell m} \sqrt{C_{\ell}^{\phi\phi}}$, $\langle x^2 \rangle = 1$, $\langle y^2 \rangle = 1$ and $\langle xy \rangle = 0$, we recover the expected signal

$$\langle (a_{\ell m}^{\text{L-ISW}})^3 \rangle = 6 f_{\ell} C_{\ell}^{\text{P}} C_{\ell}^{\phi\text{T}}. \quad (\text{A.6})$$

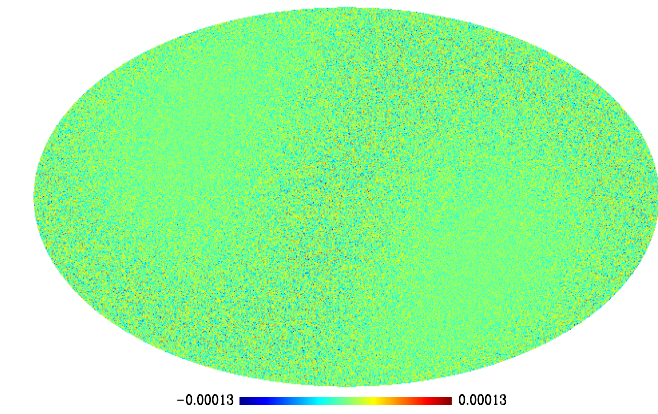
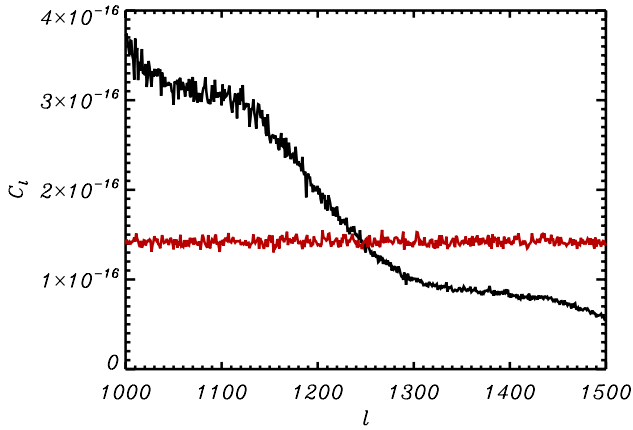


Fig. C.1. Noise simulations. Example of one simulated anisotropic noise map realization (*bottom panel*) and its correspondent noise power spectrum in red on the *upper panel*. The black line corresponds to the power spectrum from the same L-ISW simulation.

Appendix B: L-ISW cross-correlation coefficients

The definition of the CMB lensing-ISW/RS cross-correlation coefficients is (Spergel & Goldberg 1999; Verde & Spergel 2002; Giovi et al. 2005):

$$C_\ell^{T\phi} \equiv \langle \phi_{L\ell}^{*m} a_\ell^m \rangle \simeq 2 \int_0^{z_{\text{ls}}} \frac{r(z_{\text{ls}}) - r(z)}{r(z_{\text{ls}})r(z)^3} \left[\frac{\partial}{\partial z} P_\phi(k, z) \right]_{k=\frac{\ell}{r(z)}} dz. \quad (\text{B.1})$$

where, $r(z)$ is the co-moving conformal distance and $P_\phi(k, z)$ is the gravitational potential power spectrum that accounts for both the linear and non-linear contributions. The non-linear regime RS contribution to the signal is tiny, in agreement with Lewis (2012) and Junk & Komatsu (2012)². Considering both the linear ISW and the Rees Sciama effect improves the $f_{\text{NL}}^{\text{L-ISW}}$ variance and signal-to-noise ratio by a few percent ($\simeq 2\%$) with respect to the linear-only case calculation. In this work we considered both contributions for completeness. As a template for both the simulations and the estimator, we used the late ISW-lensing

² We found that the amplitude on the non-linear effect estimated in Mangilli & Verde (2009) (as well as probably in Giovi et al. 2005) compared to Lewis (2012); Junk & Komatsu (2012) was due to an interpolation problem. Even a small numerical effect at the interpolation scale $k = \frac{\ell}{r(z)}$ can propagate through the line-of-sight integration to a relevant effect on the non-linear transition scale of the $C_\ell^{T\phi}$. Note, however, that the $C_\ell^{T\phi}$ coefficients are very sensitive to the cosmology parameters related to the late-time evolution, Ω_Λ , w , σ_8 , and to the modeling of the non-linearities (e.g. Verde & Spergel (2002)), so extra care must be taken when comparing results from different authors.

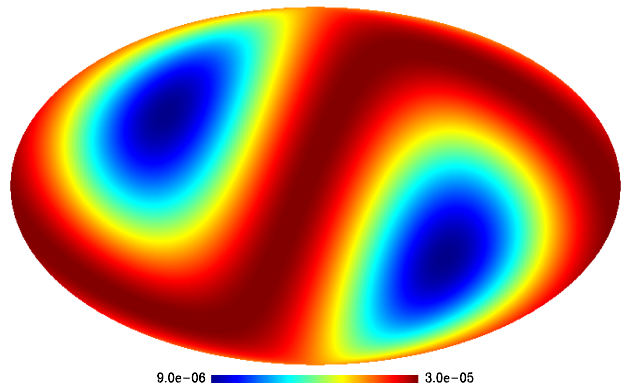
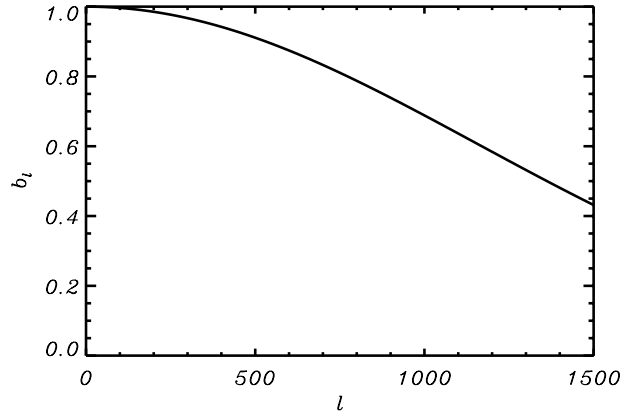


Fig. C.2. Experimental setting: beam window function and anisotropic noise map. The Gaussian beam with a 7' FWHM is shown in the *upper panel*, while the *bottom panel* shows the dipole-like anisotropic noise covariance matrix map.

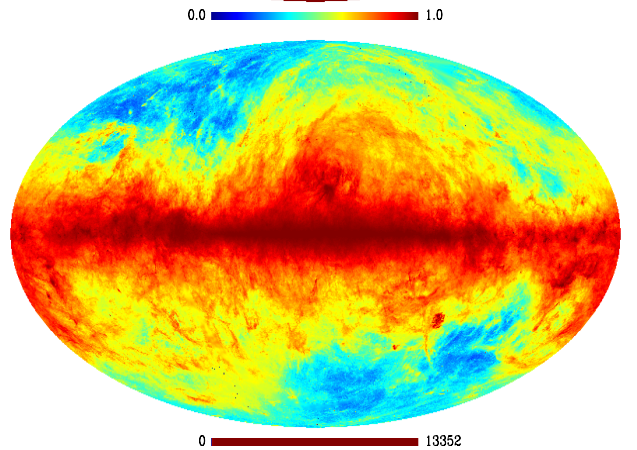
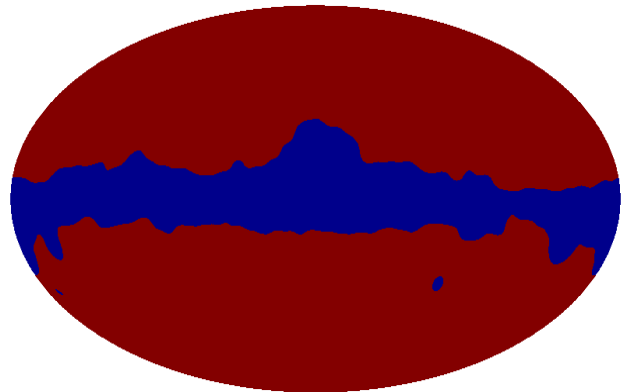


Fig. C.3. Mask. Galactic mask cut with $f_{\text{sky}} = 0.78$ (*upper panel*) obtained from thresholding the smoothed 100 μm IRAS map (*bottom panel*).

cross-correlation coefficients of Eq. (B.1). This is a good approximation since this effect provides the main contribution. However, for a detailed description see Lewis (2012).

Appendix C: experimental setting

Figures C.2 and C.3 summarize the experimental settings used in the simulations. These settings are inspired by a space-based experiment such as WMAP or *Planck*, with a variation of the noise with the ecliptic latitude. We considered a one-channel CMB experiment with a Gaussian beam with a FWHM $\theta_b = 7'$, a galactic mask leaving $\approx 80\%$ of the sky and anisotropic uncorrelated noise. In particular, we obtained a galactic type mask from the IRAS³ 100 μm map smoothed at 5 angular degrees resolution and with a threshold of 12 MJy/sr. We considered a dipole-type anisotropic noise covariance matrix, which accounts for the anisotropies owing to, e.g., the scanning strategy. An example of an anisotropic noise realization and the corresponding power spectrum is given in the bottom and upper panels of Fig. C.1. The noise starts to dominate from $\ell \simeq 1300$.

References

- Babich, D. 2005, Phys. Rev. D, 72, 043003
 Elsner, F., & Wandelt, B. D. 2013, A&A, 549, A111
 Fergusson, J., Liguori, M., & Shellard, E. 2010, Phys. Rev. D, 82, 023502
 Giovi, F., Baccigalupi, C., & Perrotta, F. 2005, Phys. Rev. D, 71, 103009
 Goldberg, D. M., & Spergel, D. N. 1999, Phys. Rev. D, 59, 103002
 Gorski, K., Hivon, E., Banday, A., et al. 2005, ApJ, 622, 759
 Hanson, D., Smith, K. M., Challinor, A., & Liguori, M. 2009, Phys. Rev. D, 80, 083004
 Junk, V., & Komatsu, E. 2012, Phys. Rev. D, 85, 123524
 Kim, J., Rotti, A., & Komatsu, E. 2013, J. Cosmol. Astropart. Phys., 4, 21
 Komatsu, E. 2010, Class. Quant. Grav., 27, 124010
 Komatsu, E., Spergel, D. N., & Wandelt, B. D. 2005, ApJ, 634, 14
 Komatsu, E., Smith, K. M., Dunkley, J., et al. 2011, ApJS, 192, 18
 Lavaux, G., & Wandelt, B. D. 2010, ApJS, 191, 32
 Lewis, A. 2012, JCAP, 1206, 023
 Lewis, A., Challinor, A., & Lasenby, A. 2000, ApJ, 538, 473
 Lewis, A., Challinor, A., & Hanson, D. 2011, JCAP, 1103, 018
 Mangilli, A., & Verde, L. 2009, Phys. Rev. D, 80, 123007
 Munshi, D., Valageas, P., Cooray, A., & Heavens, A. 2011, MNRAS, 414, 3173
 Planck Collaboration 2011, A&A, 536, A1
 Planck Collaboration 2013a, A&A, submitted [[arXiv:1303.5084](https://arxiv.org/abs/1303.5084)]
 Planck Collaboration 2013b, A&A, submitted [[arXiv:1303.5079](https://arxiv.org/abs/1303.5079)]
 Rees, M. J., & Sciama, D. W. 1968, Nature, 217, 511
 Sachs, R. K., & Wolfe, A. M. 1967, ApJ, 147, 73
 Smith, K. M., & Zaldarriaga, M. 2011, MNRAS, 417, 2
 Spergel, D. N., & Goldberg, D. M. 1999, Phys. Rev. D, 59, 103001
 Taylor, A., & Watts, P. 2001, MNRAS, 328, 1027
 The CORe Collaboration, Armitage-Caplan, C., Avillez, M., et al. 2011, white paper [[arXiv:1102.2181](https://arxiv.org/abs/1102.2181)]
 Verde, L., & Spergel, D. N. 2002, Phys. Rev. D, 65, 043007
 Yadav, A. P., & Wandelt, B. D. 2010, Adv. Astron., 2010, 565248

³ <http://www.cita.utoronto.ca/~mamd/IRIS/IrisOverview.html>